Bioelectrochemistry and Biosensors
https://www.sciltp.com/journals/bebs

Review

Impact of Polymer Microstructure and Free Volume on Electrochemical Biosensor Functionality

Taras Kavetskyy [1,2,3]

[1] Department of Physics and Information Systems & Department of Biology and Chemistry, Drohobych Ivan Franko State Pedagogical University, 82100 Drohobych, Ukraine; kavetskyy@yahoo.com
[2] South Ukrainian National Pedagogical University named after K.D. Ushynsky, 65020 Odesa, Ukraine
[3] Institute of Physics, Slovak Academy of Sciences, 84511 Bratislava, Slovakia

How To Cite: Kavetskyy, T. Impact of Polymer Microstructure and Free Volume on Electrochemical Biosensor Functionality. *Bioelectrochemistry and Biosensors* **2026**, *1*(1), 7.

Received: 3 April 2026
Revised: 17 April 2026
Accepted: 22 April 2026
Published: 27 May 2026

Abstract: This review presents a comprehensive and quantitatively oriented analysis of the role of polymer microstructure and free volume in governing the performance of electrochemical biosensors. Particular emphasis is placed on the application of positron annihilation spectroscopy (PAS) as a uniquely sensitive technique for probing sub-nanometer free-volume characteristics and establishing direct structure–function relationships. By integrating results from organic-inorganic hybrid ureasil-based and photocross-linked polymers, a consistent correlation is demonstrated between free-volume parameters (size, distribution, and thermal expansion) and key biosensor characteristics, including sensitivity, mass transport efficiency, and enzyme activity. It is shown that variations in free-volume cavity size and connectivity systematically control analyte diffusion, enzyme accessibility, and reaction kinetics within polymer matrices. Furthermore, the combined influence of network topology (crosslinking density, phase separation) and chemical functionality (polymer composition, photoinitiator effects) on free-volume evolution during polymerization and aging is elucidated. *In-situ* PAS studies of photopolymerization reveal that kinetic pathways directly determine the final microstructure and, consequently, the functional performance of biosensing platforms. Based on these insights, a generalized framework is proposed in which free volume acts as a key design parameter linking nanoscale polymer structure to macroscopic electrochemical response. This approach provides a rational basis for engineering polymer matrices for biosensors with optimized sensitivity, selectivity, and operational stability, offering new directions for the development of next-generation biosensors.

Keywords: polymers; microstructure; free volume; positron annihilation; biosensors

1. Introduction

The rapid advancement of modern sensing technologies increasingly relies on the development of materials with precisely tunable physicochemical properties. In particular, electrochemical biosensors, widely used in environmental monitoring, medical diagnostics, and biotechnological processes, demand functional materials that can simultaneously ensure high sensitivity, selectivity, and operational stability. Among the available material platforms, polymers have emerged as exceptionally versatile candidates due to their structural diversity, ease of processing, and ability to form tailored microenvironments for biological recognition elements.

In electrochemical biosensors, polymer-based matrices play a central role by enabling the immobilization of enzymes and other biomolecules while preserving their catalytic activity and structural integrity. Beyond serving as passive supports, these matrices actively influence mass transport, interfacial charge transfer, and the spatial

Copyright: © 2026 by the authors. This is an open access article under the terms and conditions of the Creative Commons Attribution (CC BY) license (https://creativecommons.org/licenses/by/4.0/).
Publisher's Note: Scilight stays neutral with regard to jurisdictional claims in published maps and institutional affiliations.

distribution of biocatalytic reactions. Consequently, the performance of a biosensor is not determined solely by the biological component but is critically governed by the physicochemical characteristics of the surrounding polymer network.

A key yet often underappreciated parameter controlling these characteristics is the free volume within the polymer matrix. Free volume—defined as the unoccupied nanoscopic space within a material, regulates the diffusion of analytes, accessibility of active sites, and removal of reaction products. At the same time, it reflects the underlying polymer microstructure, including chain packing, crosslinking density, and the presence of nanophase-separated domains. Subtle variations in free volume can therefore lead to significant changes in transport properties and enzymatic efficiency, ultimately impacting the analytical response of the biosensor.

Despite its importance, establishing a direct and quantitative relationship between polymer microstructure and biosensor performance remains a major challenge. This difficulty arises from the multiscale nature of polymer systems, where nanoscale structural features must be correlated with macroscopic electrochemical behavior. In this context, positron annihilation spectroscopy (PAS) has emerged as a powerful and uniquely sensitive technique for probing free-volume characteristics at the atomic and sub-nanometer scale. By providing direct information on the size, distribution, and thermal behavior of free-volume cavities, PAS enables a detailed understanding of structure–property relationships that are otherwise inaccessible using conventional methods.

Recent advances in polymer science, including the development of hybrid organic–inorganic networks, photopolymerizable systems, and nanocomposites, have further expanded the design space for biosensor materials. These systems exhibit complex microstructures in which free volume is strongly influenced by composition, crosslinking mechanisms, and external stimuli such as temperature and irradiation. At the same time, emerging evidence suggests that both topological factors (related to network architecture and free-volume connectivity) and chemical factors (such as polymer charge and functional groups) jointly determine biosensor performance.

This review aims to provide a comprehensive analysis of the role of polymer microstructure and free volume in electrochemical biosensor functionality. Particular emphasis is placed on the application of positron annihilation spectroscopy as a tool for elucidating free-volume properties and linking them to key analytical parameters, including sensitivity, apparent Michaelis–Menten constants, and linear detection ranges. By integrating insights from ureasil-based systems, photochemically crosslinked polymers, and hybrid nanocomposites, this work identifies general principles governing enzyme immobilization, mass transport, and signal generation.

Ultimately, understanding and controlling free volume in polymer matrices offers a rational pathway toward the design of next-generation biosensors with enhanced performance. The concepts discussed herein establish a unified framework that connects nanoscale polymer structure with macroscopic device functionality and highlight opportunities for the targeted engineering of advanced sensing platforms.

2. Investigation of Free Volume in Polymer Matrices Using Positron Annihilation Spectroscopy (PAS)

The free volume in polymeric materials plays a critical role in the design of electrochemical biosensors, as it directly influences the spatial and energetic characteristics of adsorption centers within meso- and nanopores. Ensuring optimal geometrical and energetic properties of these adsorption sites is an essential step in achieving high-performance biosensors. Consequently, the fabrication process must account for the structural features related to free volume and adsorption properties within the polymer matrix.

A highly precise and non-destructive technique for probing free volume at the atomic and sub-atomic scale is positron annihilation spectroscopy (PAS) by using positron annihilation lifetime measurements. PAS also allows the study of temperature-dependent ortho-positronium (*o*-Ps) behavior during heating–cooling cycles. Beyond pore sizes, this method provides information on phase transitions, glass transition temperature (T_g), and thermal expansion coefficients of free-volume nanopores above and below T_g [1]. Measurements were conducted for ureasil and photopolymer matrices.

A series of organically modified ureasil polymer samples was prepared by mixing two precursors: Precursor 1 (long chains): ICPTES + Jeffamine ED-600; and Precursor 2 (short chains): ICPTES + APTES, with the following ratios shown in Table 1 [2].

Table 1. The ratios of Precursor 1 and Precursor 2 in the studied ureasil polymer samples.

Sample	Precursor 1 (mol%)	Precursor 2 (mol%)
1	100	0
2	56.6	43.4
3	30.8	69.2
4	12.7	87.3
5	0	100

Based on the structural model for sample 1 [3], a morphological model was constructed in accordance with SAXS results (Figure 1). Siloxane clusters (red spheres) assemble into domains, forming a two-level hierarchical structure. The primary level consists of siloxane nanoclusters formed via polycondensation at polymer chain ends, whereas the secondary level comprises high-electron-density domains where siloxane clusters are separated by low-density organic phases. Polymer chains are folded within domains and nearly stretched between them.

Adding Precursor 2 disrupts spatial correlation of silica-rich Phase 1 by forming Phase 2 (violet spheres), which displaces silica particles and diminishes structural correlation. Pure Precursor 2 exhibits slightly correlated particles (~5 nm^{-1} peak) and randomly distributed particles (broad low-q band). This schematic provides a clear molecular-level visualization of polymer–nanoparticle interactions and the impact on free-volume distribution, critical for biosensor performance.

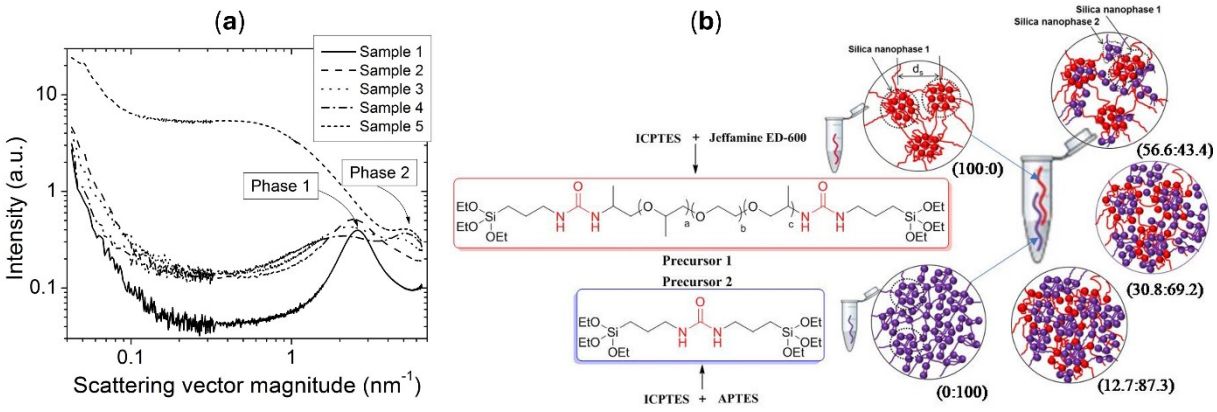

Figure 1. (**a**) Scattering intensity as a function of the scattering vector for mixtures prepared with different Precursor 1/Precursor 2 ratios. (**b**) Morphological model of the structure of samples obtained from Precursor 1 (Sample 1—100:0), Precursor 2 (Sample 5—0:100) and intermediate mixtures (Sample 2—56.6:43.4, Sample 3—30.8:69.2, and Sample 4—12.7:87.3). Adapted from [2].

The temperature dependences of the ortho-positronium (*o*-Ps) lifetime for the studied samples are presented in Figure 2. These temperature profiles reveal several important features discussed below. In particular, a significant decrease in the thermal expansion of free-volume cavities above the glass transition temperature (T_g) is observed with increasing content of precursor 2 (short organic chains) (Table 2). This effect is especially evident in samples containing a larger inorganic fraction, i.e., those enriched with a silica nanophase. Within the framework of positron annihilation spectroscopy (PAS), T_g can be determined as the intersection point of the slopes in the temperature dependence of the free-volume hole size, $V_h(T)$. As the concentration of precursor 2 increases, the T_g value shifts toward higher temperatures, and for sample 5 it could not be reliably determined.

The influence of physical aging on the microstructural characteristics of free volume in polymers was investigated using pure ureasil samples and their composites with chalcogenide clusters (As_2S_3) as model systems. Figure 3 shows the temperature dependence of the ortho-positronium (*o*-Ps) lifetime for ureasil-based materials, including pure ureasil (K0-fresh and K0-aged) and the ureasil/As_2S_3 composite (K4-fresh and K4-aged). In this context, the "fresh" samples correspond to materials analyzed two months after synthesis, while the "aged" samples were measured one year after synthesis. All samples were stored at room temperature prior to the measurements. The temperature dependences were recorded in the range of 15–350 K.

The temperature at which a change in the slope of the free-volume dependence (ortho-positronium, *o*-Ps lifetime) is observed corresponds to the primary glass transition temperature, T_{g1}. The determined values of the free-volume cavity size V_{h1}, calculated using a spherical approximation at T_{g1}, along with the thermal expansion coefficients of the free-volume cavities below and above T_{g1} (α_{F1} and α_{F2}, respectively), as well as the swelling in ethanol (EtOH), are summarized in Table 3. A lower temperature at which the slope of $V_h(T)$ also changes is, in some cases, observed and denoted as T_{g2} (sub-glass transition [4]) for the aged K0 sample. Both T_{g1} and T_{g2} are observed for the fresh and aged K4 composites. Furthermore, it was found that the free-volume changes depend on the thermal history, showing hysteresis between cooling and heating cycles for the aged ureasil/As_2S_3 samples.

Clear differences in the behavior of the polymer network are observed for aged samples, as well as the influence of chalcogenide (As_2S_3) particles on the free volume of the ureasil polymer network. Comparing the results summarized in Table 3, it is evident that the most pronounced changes in the microscopic characteristics of free volume, represented by α_{F1} and α_{F2}, as well as swelling (reflecting chain cross-linking density), are observed for the fresh ureasil/As_2S_3 sample.

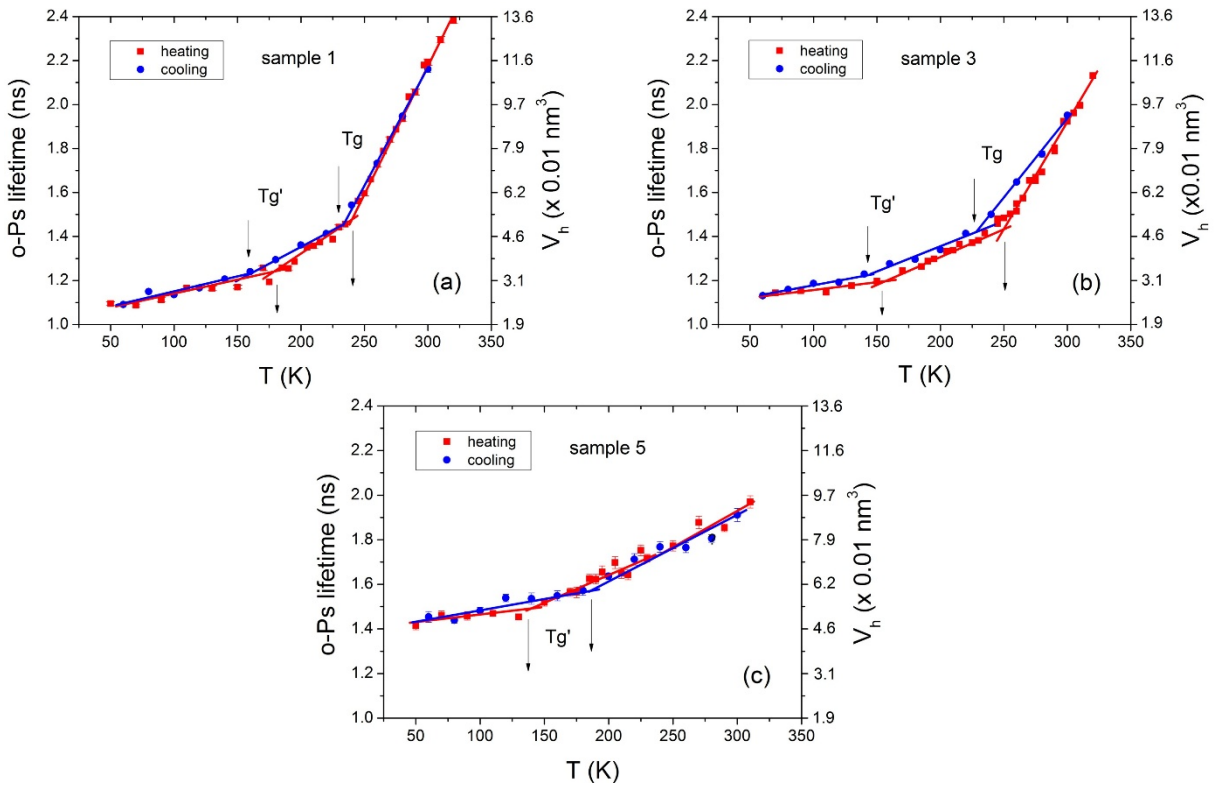

Figure 2. Temperature dependence of the ortho-positronium (*o*-Ps) lifetime in ureasil samples: (**a**) sample 1, (**b**) sample 3, and (**c**) sample 5. The free-volume cavity size $V_h = 4/3\pi R_h^3$, where the radius R_h was calculated using the Tao-Eldrup equation, is shown on the right vertical axis. Adapted from [2].

Table 2. Glass transition temperatures (T_g) and sub-glass transition temperatures (T_g'), free-volume cavity size V_h at T_g, slopes of the $V_h(T)$ dependences below and above T_g (α_{F1} and α_{F2}, respectively), their difference ($\alpha_{F2} - \alpha_{F1}$), and swelling characteristics in ethanol (S_{sat}—initial saturation value, S_{max}—maximum saturation value) for the investigated ureasil polymers measured during heating and cooling cycles [2]. Sample designations (as in Figure 2) are described in the text above.

Sample	T_g (K)	T_g' (K)	$V_h(T_g)$ (nm³)	α_{F1} (10^{-4} K^{-1})	α_{F2} (10^{-4} K^{-1})	$\alpha_{F2} - \alpha_{F1}$ (10^{-4} K^{-1})	S_{sat}/S_{max} (%)
Sample 1, heating	239 ± 14	169 ± 37	0.050 ± 0.009	53 ± 11	213 ± 40	160	36.2/37.8
Sample 1, cooling	232 ± 21	156 ± 26	0.050 ± 0.005	44 ± 5	181 ± 20	137	–
Sample 3, heating	250 ± 20	153 ± 31	0.049 ± 0.005	39 ± 5	163 ± 19	124	19.6/22.3
Sample 3, cooling	231 ± 28	143 ± 79	0.048 ± 0.010	34 ± 9	131 ± 27	97	–
Sample 5, heating	n/a	137 ± 50	n/a	n/a	n/a	n/a	9.3/–
Sample 5, cooling	n/a	184 ± 83	n/a	n/a	n/a	n/a	–

Figure 4 shows the free-volume cavity size, V_h, calculated from the ortho-positronium (*o*-Ps) lifetime, for photocross-linked polymers ELO/10RD and ELO/30RD as a function of temperature in the range 15–350 K. The photopolymer matrix consisted of epoxidized linseed oil (ELO), diglycidyl ether of bisphenol A (RD) as the reactive diluent, and a 50% solution of triarylsulfonium hexafluorophosphate in propylene carbonate as the photoinitiator (PI). The polymers were synthesized by reacting ELO with either 10 mol% or 30 mol% RD, using 3 mol% PI, resulting in the ELO/10RD and ELO/30RD networks, respectively.

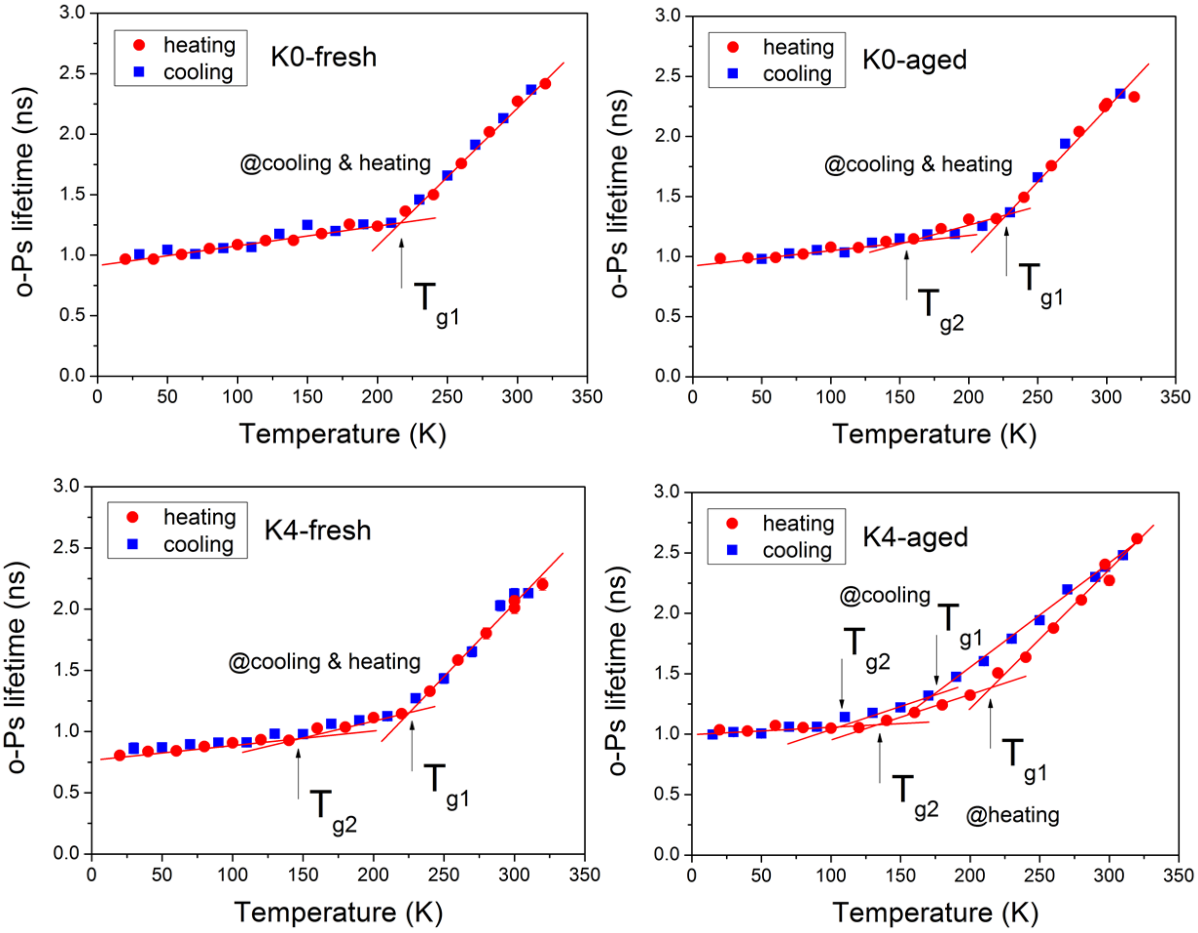

Figure 3. Temperature dependence of the ortho-positronium (*o*-Ps) lifetime in ureasil-based samples: ureasil (K0-fresh and K0-aged) and ureasil/As_2S_3 composite (K4-fresh and K4-aged) measured during cooling and heating cycles. Error bars are within the size of the symbols. Adapted from [5].

In both polymer systems, the free-volume cavity size shows hysteresis, depending on the heating or cooling cycle. Values of V_h at T_g, swelling capacity in ethanol (S), and the slopes of $V_h(T)$ below and above T_g (α_{F1} and α_{F2}), as well as their difference, are summarized in Table 4. Notably, the average free-volume cavity size in ELO/10RD is larger than in ELO/30RD. Furthermore, ELO/10RD exhibits a greater difference between the thermal expansion coefficients of free-volume cavities below and above T_g compared with ELO/30RD, indicating a lower cross-linking density and higher polymer chain mobility in the former.

Table 3. Primary glass transition (T_{g1}) and sub-glass transition (T_{g2}) temperatures, free-volume cavity size at T_{g1} (V_{h1}), slopes of the $V_h(T)$ dependence below and above T_{g1} (α_{F1} and α_{F2}, respectively), their difference ($\alpha_{F2} - \alpha_{F1}$), and ethanol swelling (S) for the investigated ureasil-based polymers measured during cooling and heating cycles [5]. Sample designations (as in Figure 3) are provided in the text above.

Sample	T_{g1} (K)	T_{g2} (K)	V_{h1} (nm³)	α_{F1} ($T < T_{g1}$) (10^{-4} K^{-1})	α_{F2} ($T > T_{g1}$) (10^{-4} K^{-1})	$\alpha_{F2} - \alpha_{F1}$ (10^{-4} K^{-1})	S (%)
K0-fresh (cooling & heating)	216 ± 13	–	0.123 ± 0.002	25 ± 3	286 ± 21	261	23.0
K0-aged (cooling & heating)	230 ± 19	166 ± 89	0.123 ± 0.003	53 ± 22	273 ± 99	220	11.0
K4-fresh (cooling & heating)	227 ± 18	126 ± 38	0.104 ± 0.001	48 ± 10	344 ± 63	296	24.0
K4-aged (cooling)	178 ± 19	88 ± 58	0.134 ± 0.001	46 ± 17	206 ± 56	160	19.0
K4-aged (heating)	228 ± 38	130 ± 38	0.123 ± 0.004	56 ± 22	237 ± 84	181	–

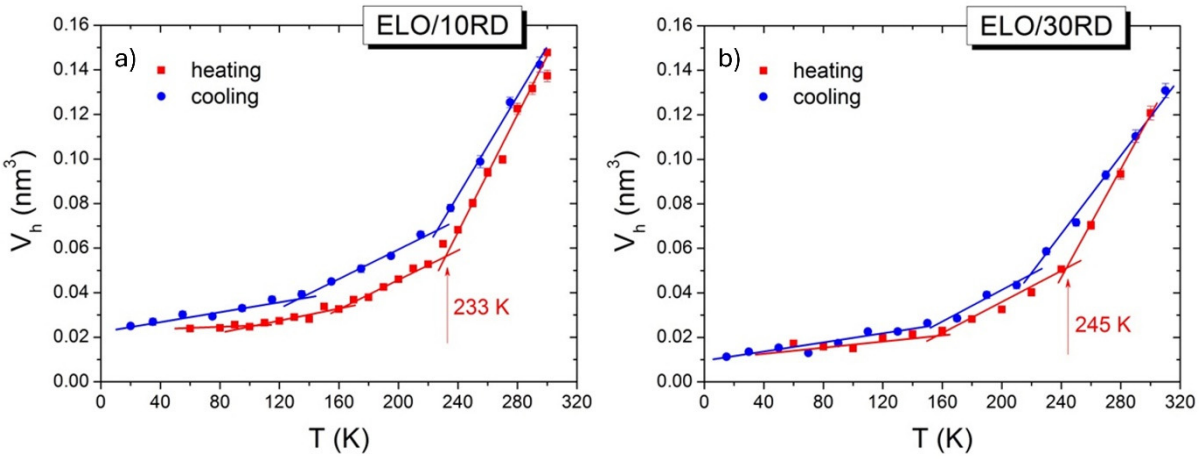

Figure 4. Temperature dependence of the free-volume cavity size, V_h, calculated from the ortho-positronium (*o*-Ps) lifetime for photocross-linked polymers ELO/10RD (**a**) and ELO/30RD (**b**) during cooling and heating cycles. Adapted from [6].

Table 4. Glass transition temperature (T_g), free-volume cavity size (V_h) at T_g, slopes of the $V_h(T)$ dependence below and above T_g (α_{F1} and α_{F2}, respectively), their difference ($\alpha_{F2} - \alpha_{F1}$), and swelling capacity (S) in ethanol for photochemically cross-linked polymers. Values for heating and cooling cycles are indicated in the upper and lower parts of each column, respectively [6].

Sample	T_g (K)	V_h (nm³)	α_{F1} ($T < T_g$) (10^{-4} K^{-1})	α_{F2} ($T > T_g$) (10^{-4} K^{-1})	$\alpha_{F2} - \alpha_{F1}$ (10^{-4} K^{-1})	S (%)
ELO/10RD	233	0.057 ± 0.002 0.068 ± 0.002	3.53 ± 0.30 3.31 ± 0.32	13.02 ± 0.60 11.16 ± 0.55	9.49 ± 0.67 7.85 ± 0.64	24.09
ELO/30RD	245	0.051 ± 0.002 0.049 ± 0.002	3.47 ± 0.33 3.87 ± 0.83	12.42 ± 0.64 8.96 ± 0.48	8.95 ± 0.72 5.09 ± 0.96	24.81

2.1. In-Situ Photopolymerization and Photodegradation of Cured Polymer Matrices

In this section, in-situ photopolymerization and photodegradation processes of cured polymer matrices were investigated. Samples were prepared from mixtures of acrylated epoxidized soybean oil (AESO) and vanillin dimethacrylate (VDM), both in the presence and absence of the photoinitiator 2,2-dimethoxy-2-phenylacetophenone (DMPA). It was found that the nanopore size and the relative free-volume fraction among the AESO/VDM, ELO/PI, ELO/10RD1/PI, and AESO/VDM/DMPA samples were highest for AESO-based matrices without a photoinitiator and lowest for AESO-based samples containing the photoinitiator (Figure 5).

The kinetics of photopolymerization were studied for AESO:VDM samples with monomer molar ratios of 1:0, 1:0.25, 1:0.5, and 1:1, both with and without the photoinitiator DMPA. In-situ monitoring of the reaction progress was performed using positron annihilation spectroscopy (PAS) under periodic illumination for AESO/VDM samples with varying VDM concentrations and in the presence or absence of PI (Figure 6). The results revealed that samples containing the photoinitiator exhibited a faster reduction in local free volume (LFV) compared to samples without PI. Furthermore, increasing the VDM concentration slowed down the cross-linking process, indicating a retardation of network formation with higher VDM content.

To investigate the reaction progress, the early stages of photopolymerization were also monitored under continuous illumination using a thermocouple (TC) in the same sample geometry as in the PAS measurements (Figure 7). It was observed that increasing the VDM concentration in AESO-based samples, both with and without the photoinitiator (PI), accelerates the initial reaction, reflecting more or less pronounced phase separation as indicated by the induction period t_{IP} (Table 5). However, the increase in t_{max} values for the AESO/VDM series, with or without PI, confirmed that higher VDM content ultimately slows down the overall reaction. Thus, both TC and PAS measurements consistently showed the slowest reaction kinetics for the AESO/VDM sample with the highest VDM concentration.

Next, a comparison of free-volume characteristics (PAS), double-bond conversion (FTIR), and water sorption–desorption experiments with diffusion coefficient evaluation were carried out for cured AESO-based samples with and without the photoinitiator (PI).

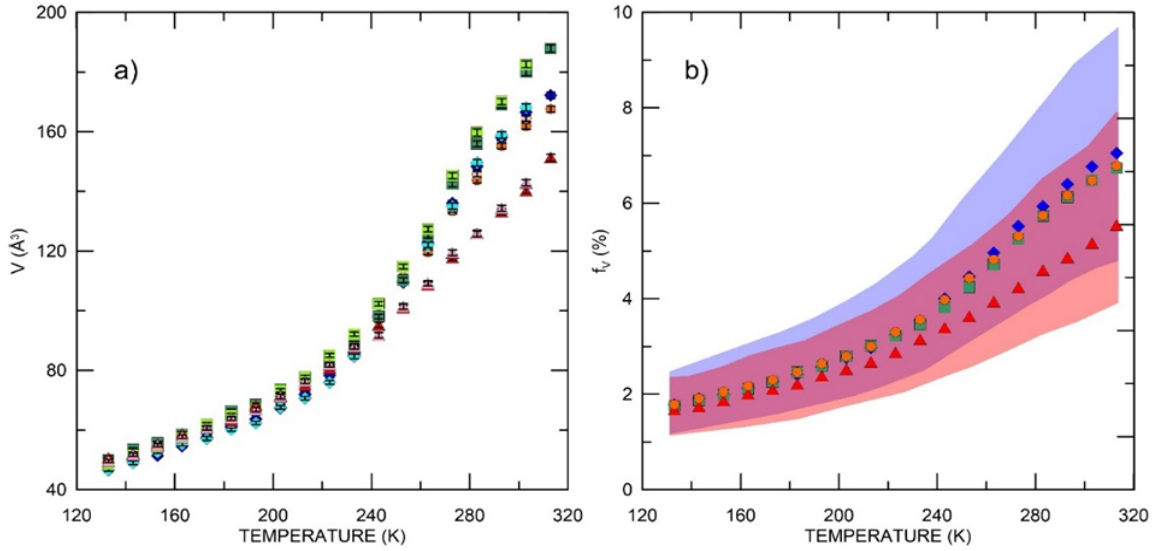

Figure 5. Free volume V (**a**) and relative free-volume fraction $f_V = CI_3V$ (where I_3 is the *o*-Ps intensity and C is a parameter ranging from 0.001 to 0.002 depending on the material) (**b**) as a function of temperature during heating: ELO/PI—orange circles, ELO/10RD1/PI—dark blue diamonds, AESO/VDM—dark green squares, AESO/VDM/DMPA—red triangles; and during cooling: ELO/PI—beige circles, ELO/10RD1/PI—light blue diamonds, AESO/VDM—light green squares, AESO/VDM/DMPA—pink triangles. On the right panel, symbols correspond to C = 0.0014 for the polymers. Shaded areas in blue and red indicate the range of results for ELO/PI and AESO/VDM/DMPA, respectively, for C values between 0.001 and 0.002. Adapted from [7].

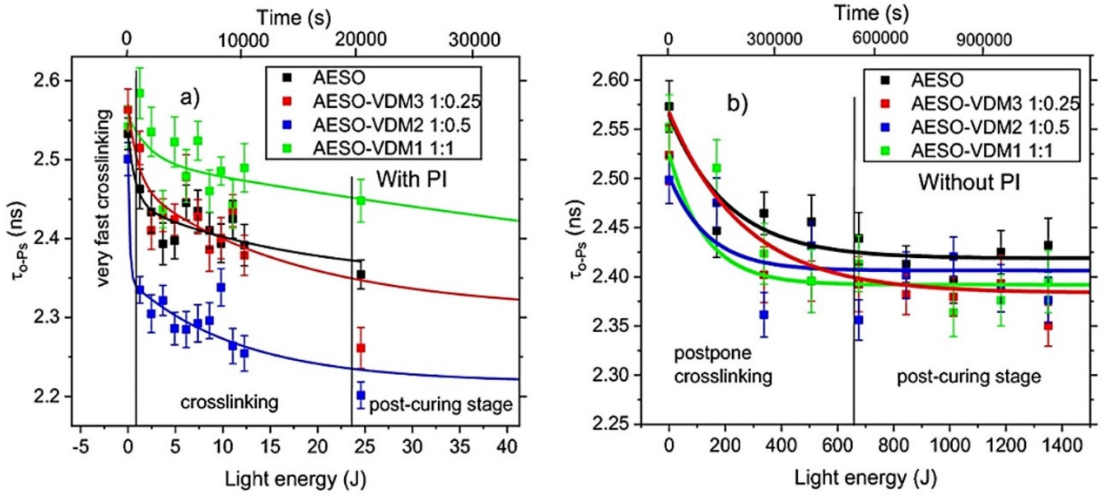

Figure 6. Photopolymerization progress for samples with (**a**) and without (**b**) photoinitiator (PI), monitored via ortho-positronium (*o*-Ps) lifetime measurements. Two X-axes are shown: total irradiation time as "Time" (upper X-axis) and the light energy absorbed within the sample volume as "Light Energy" (lower X-axis). Adapted from [8].

With increasing vanillin dimethacrylate (VDM) content, the free-volume cavity size in all cured samples decreased from 0.133 to 0.118 nm^3 in the presence of PI and from 0.144 to 0.131 nm^3 without PI (Table 6). Samples containing the photoinitiator exhibited smaller free-volume sizes in the cured state compared to samples without PI, indicating that the photoinitiator influences not only the rate of photopolymerization but also the final microstructural properties of the cured material. This behavior can be explained by the transformation of long polymer chains into shorter ones via bond cleavage during photopolymerization, which occurs more efficiently in the presence of a photoinitiator. This hypothesis is supported by the significant reduction in free-volume sizes observed in ureasil-based polymers dominated by precursor 2 (short chains), as shown in Figure 2 (sample 5).

PAS measurements also revealed heterogeneous cross-linking across the sample thickness for 3 mm-thick samples containing PI, with differences between the side facing the light source and the opposite side. This observation is attributed to differential light absorption within the material. UV light absorption leads to varying light intensity in the reaction zone, resulting in different cross-linking rates. This effect was most pronounced in samples with PI due to the two-phase nature of the reduction in ortho-positronium (*o*-Ps) lifetime. On the side

exposed to higher light intensity, cavities were smaller and likely more numerous, as indicated by higher *o*-Ps formation intensity. Furthermore, increasing the VDM content amplified the structural heterogeneity between the illuminated and opposite sides of the samples.

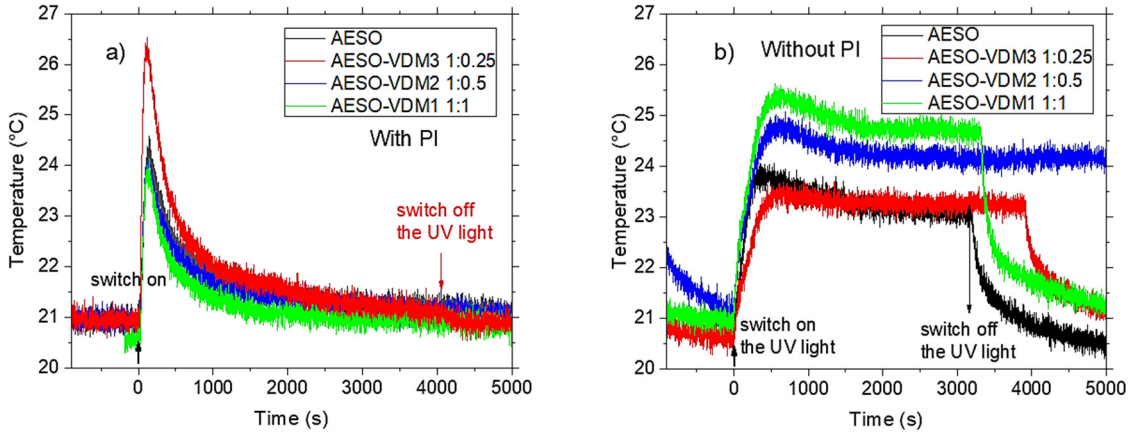

Figure 7. Reaction temperature as a function of time for AESO-based samples with photoinitiator (PI) (**a**) and without PI (**b**). Ultraviolet (UV) light was turned on at 0 s. The second arrow indicates the time when the UV light was turned off (shown for only one sample for clarity). For the AESO-VDM 1:0.5 sample without PI, the light was turned off slightly after 4000 s, outside the displayed time scale, so the corresponding temperature jump is not visible. Adapted from [8].

Infrared (IR) spectroscopy showed that increasing the concentration of VDM leads to a decrease in the conversion of C=C double bonds (absorption band at 6172 cm^{-1}) for both types of polymer samples, with and without PI (Figure 8).

Table 5. Characteristic induction time at the inflection point t_{IP} and the time of maximum reaction rate t_{max}, corresponding to the maximum and zero-crossing of the first derivative of the temperature vs. time curve (dT/dt), respectively [8].

Sample	t_{IP} (s)	t_{max} (s)
With photoinitiator (PI)		
AESO	58	144
AESO-VDM 1:0.25 (VDM3)	37	108
AESO-VDM 1:0.5 (VDM2)	48	112
AESO-VDM 1:1 (VDM1)	49	118
Without photoinitiator (PI)		
AESO	30	400
AESO-VDM 1:0.25 (VDM3)	28	595
AESO-VDM 1:0.5 (VDM2)	28	620
AESO-VDM 1:1 (VDM1)	28	650

Table 6. Characteristic ortho-positronium (*o*-Ps) lifetimes for the liquid state (τ_0) and the final cured state (τ_f), along with the corresponding calculated local free-volume cavity size (V_h, spherical approximation) for samples with and without photoinitiator [8].

Sample	τ_0 (ns)	τ_f (ns)	V_h (nm³)
With photoinitiator (PI)			
AESO	2.53 ± 0.02	2.38 ± 0.02	0.133 ± 0.002
AESO-VDM 1:0.25 (VDM3)	2.56 ± 0.03	2.32 ± 0.03	0.127 ± 0.003
AESO-VDM 1:0.5 (VDM2)	2.50 ± 0.02	2.35 ± 0.02	0.130 ± 0.002
AESO-VDM 1:1 (VDM1)	2.54 ± 0.03	2.23 ± 0.02	0.118 ± 0.002
Without photoinitiator (PI)			
AESO	2.57 ± 0.03	2.48 ± 0.01	0.144 ± 0.001
AESO-VDM 1:0.25 (VDM3)	2.52 ± 0.03	2.37 ± 0.03	0.133 ± 0.003
AESO-VDM 1:0.5 (VDM2)	2.50 ± 0.03	2.35 ± 0.03	0.131 ± 0.003
AESO-VDM 1:1 (VDM1)	2.55 ± 0.03	2.35 ± 0.02	0.131 ± 0.003

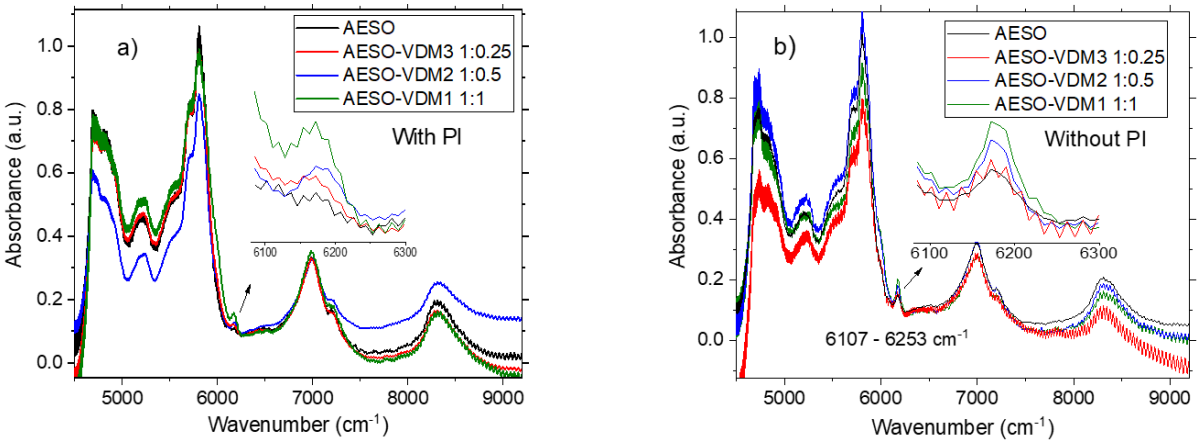

Figure 8. IR spectra of AESO-VDM polymer series: with photoinitiator (**a**) and without it (**b**). Adapted from [8].

Moreover, polymer samples containing a PI are more highly crosslinked, as evidenced by a higher conversion of C=C double bonds. From this perspective, AESO + PI should exhibit the highest conversion of double bonds and, consequently, the maximum degree of crosslinking, which is indeed observed (minimum intensity of the absorption band at 6172 cm^{-1}) [8].

2.2. Water Sorption and Desorption

It was found that an increased VDM concentration in the samples slows down the water sorption process, which correlates with the formation of reduced local free volumes in the polymer network (PN). The swelling degree (*S*), determined from the sorption curve (initial and final weight values), generally decreased with increasing VDM concentration (Figure 9).

Most likely, the presence of aromatic rings in the VDM-containing segments of the polymer network reduces the local free volume within the structure, thereby hindering water sorption in samples with higher VDM content compared to neat AESO. This explanation appears more plausible than attributing the low swelling capacity to a high crosslinking density, which in our case would contradict the results of near-IR spectroscopic analysis (Figure 8).

The water diffusion coefficients (*D*) for the investigated AESO-VDM samples were determined from sorption and desorption curves and are presented as a function of VDM content in Figure 10. The diffusion coefficient tends to decrease with increasing VDM concentration, which is consistent with the aforementioned swelling results (Figure 9).

It was concluded that VDM incorporation, as well as the presence of a photoinitiator, affects (reduces) the size of free-volume cavities, the quality of crosslinking (crosslink density), and the diffusion properties, as evaluated using water. Control over these parameters enables tuning of these polymers as an optimal matrix for the immobilization of biomolecules of various sizes (large or very small).

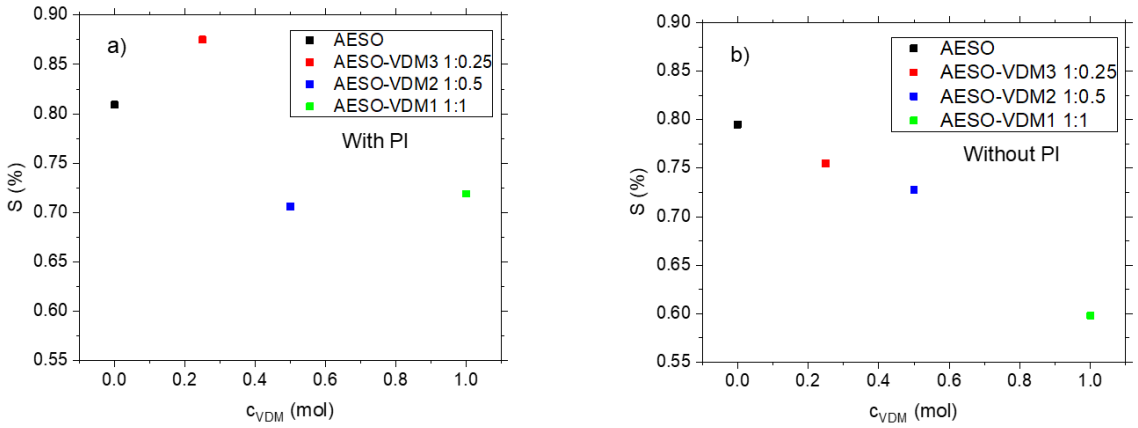

Figure 9. Dependence of the swelling parameter (*S*) on VDM concentration in AESO-VDM series samples: with photoinitiator (**a**) and without photoinitiator (**b**). Adapted from [8].

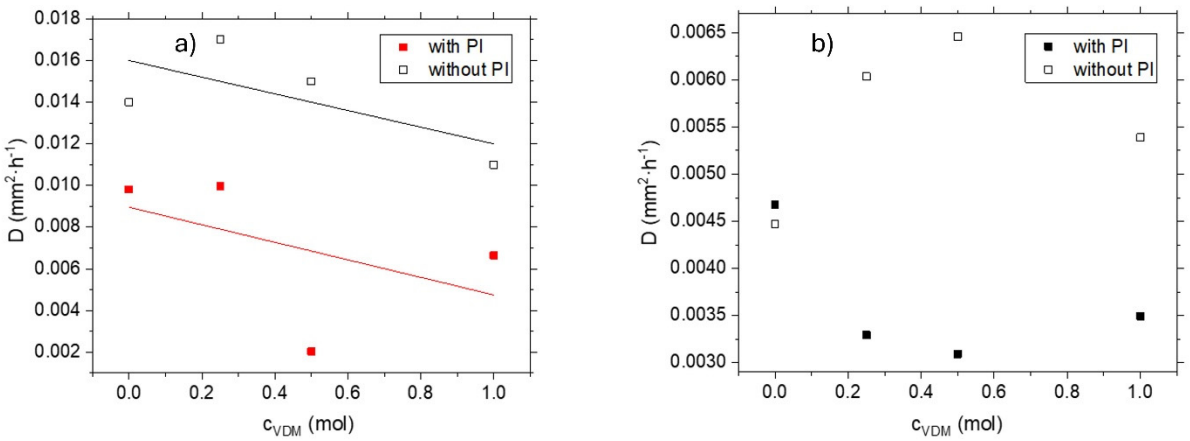

Figure 10. Dependence of the water diffusion coefficient (*D*), calculated from sorption (**a**) and desorption (**b**) curves, on VDM concentration. Adapted from [8].

The possibility of photodegradation processes was investigated by prolonged UV exposure of cured AESO:VDM (1:0.5) polymer samples. The samples were subjected to different UV irradiation times and analyzed by PAS and IR spectroscopy using the same protocol (Table 7). Samples with a thickness of 3 mm were irradiated under identical conditions for both PAS and IR spectroscopic measurements. For each sample, two separate datasets were collected: one for the lower part (facing the UV light) and one for the upper part (opposite to the light source).

Table 7. UV irradiation time protocol for the investigated AESO:VDM (1:0.5) samples [9].

Protocol	V1	V2	V3	V4	V5	V6
Irradiation period	5 h 16 min	6 h 23 min	9 h 06 min	18 h 46 min	26 h 42 min	48 h 04 min
Total irradiation time	5 h 16 min	11 h 39 min	20 h 45 min	39 h 21 min	66 h 03 min	114 h 07 min

The results obtained by PAS and IR spectroscopy for the cured samples under continuous UV irradiation are shown in Figures 11 and 12, respectively, according to the applied time protocol (Table 7). Both methods revealed that UV exposure promotes structural changes in the materials during photopolymerization and subsequent irradiation of the formed samples. These changes can be quite significant for prolonged irradiation times (increased dose), particularly in terms of photoinduced modifications of the atomic and molecular structure.

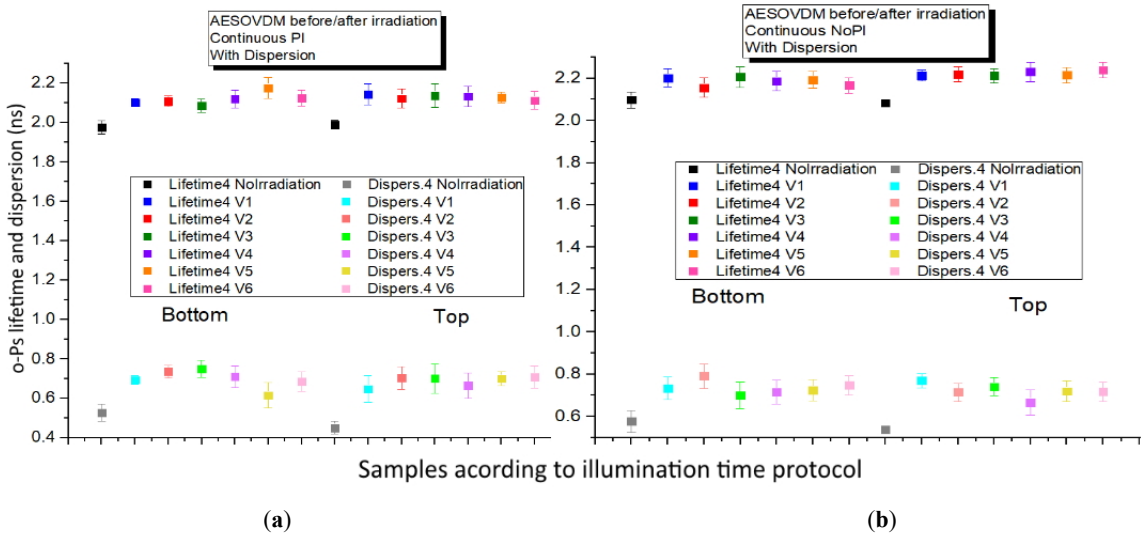

(**a**) (**b**)

Figure 11. PAS results (*o*-Ps lifetime and its dispersion) according to the UV irradiation time protocol for cured AESO:VDM (1:0.5) samples, with photoinitiator PI (**a**) and without photoinitiator PI (**b**), under continuous UV exposure. Adapted from [9].

At the same time, the different sensitivities of the applied methods to changes at the material surface can be observed. While Fourier-transform IR spectroscopy is sensitive to increases in UV irradiation dose on the side of

the sample facing the light, as it detects changes in surface area, PAS characterizes the bulk properties of the sample, since the positron energy spectrum from the ^{22}Na source is continuous.

Therefore, PAS lifetimes cannot capture changes in a thin surface layer, and the *o*-Ps lifetimes and their dispersions remain practically constant with dose (Figure 11). An exception occurs at the beginning of UV lamp irradiation, where, under the influence of intense UV light, changes in local free volume (increase) already occur throughout the bulk of the sample, accompanied by broadening of the distribution of these local free volumes. This is manifested as an increase in the dispersion of *o*-Ps lifetimes, analyzed using the LT program in continuous lifetime mode. The results indicate the presence of photodegradation in the polymer matrix.

Analysis of surface changes by Fourier-transform IR spectroscopy under continuous UV exposure reveals several notable bands in the recorded spectra (Figure 12): 1180–1200 cm^{-1} (C–O–C), 1700–1750 cm^{-1} (C=O), 2700–2900 cm^{-1} (C–H), and 3500–3600 cm^{-1} (O–H). In the sample with photoinitiator PI in direct contact with UV light during photopolymerization (“bottom”, Figure 12a), the intensity of O–H and C=O bands increases with each irradiation period, whereas the intensity of C–H and C–O–C bands decreases. This may be associated with photostructural changes within the polymer matrix due to sub-threshold radiation effects in polymers, leading to the observed changes in IR band intensities and photodegradation. Interestingly, in the PI-containing sample on the side opposite the light (“top”, Figure 12b), no such effect was observed.

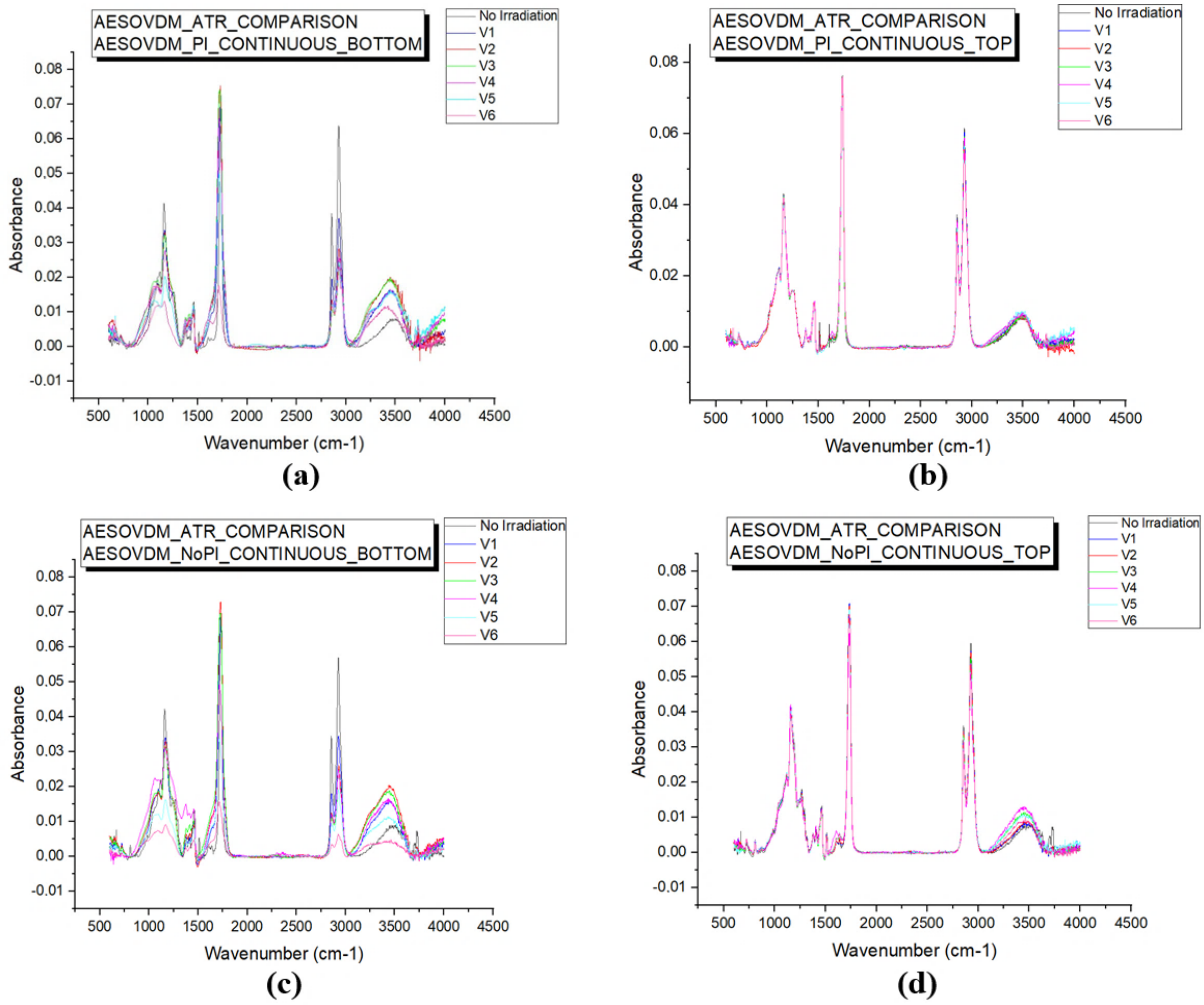

Figure 12. FTIR spectroscopy results for cured AESO:VDM (1:0.5) samples under continuous UV exposure: with PI: (**a**) in direct contact with UV light during photopolymerization “bottom”, (**b**) opposite to the light “top”; and without PI: (**c**) in direct contact with UV light during photopolymerization “bottom”, (**d**) opposite to the light “top”. Adapted from [10].

Conversely, in the sample without PI that was in direct contact with UV light during photopolymerization (“bottom”, Figure 12c), the changes in IR band intensity are even more pronounced compared to the PI-containing sample (Figure 12a), indicating a less crosslinked (less cured) structure in the absence of the photoinitiator. Meanwhile, the effect is minor for this sample on the side opposite the light (“top”, Figure 12d), showing only an increase in the O–H band intensity with each irradiation period.

The appearance and increase in intensity of carbonyl bands (C=O, 1700–1750 cm^{-1}) have also been observed in studies of polyethylene and other polymers undergoing gamma-induced oxidation [11,12], providing direct evidence of oxidative degradation. Accordingly, our results can also be interpreted as photoinduced oxidative degradation within the framework of the main principles of sub-threshold radiation effects in polymers. Such oxidative degradation is controllable and can be mitigated or enhanced depending on the presence or absence of a photoinitiator.

EPR spectroscopy results for cured AESO:VDM (1:0.5) samples containing PI during UV irradiation and dark periods are shown in Figure 13. A gradual decrease in the concentration of free radicals was observed during dark periods of 3 and 6 min, indicating that the free radical population decreases over time in the absence of light. The presence of free radicals may be attributed to the photoinitiator acting as a radical source for photopolymerization, as well as to photostructural transformations occurring during polymer photodegradation.

The EPR data indicate that UV exposure leads to the maximum formation of free radicals due to photoinitiator activation, whereas in the absence of light, the radicals gradually decay via polymerization and termination reactions, resulting in a decrease in their concentration.

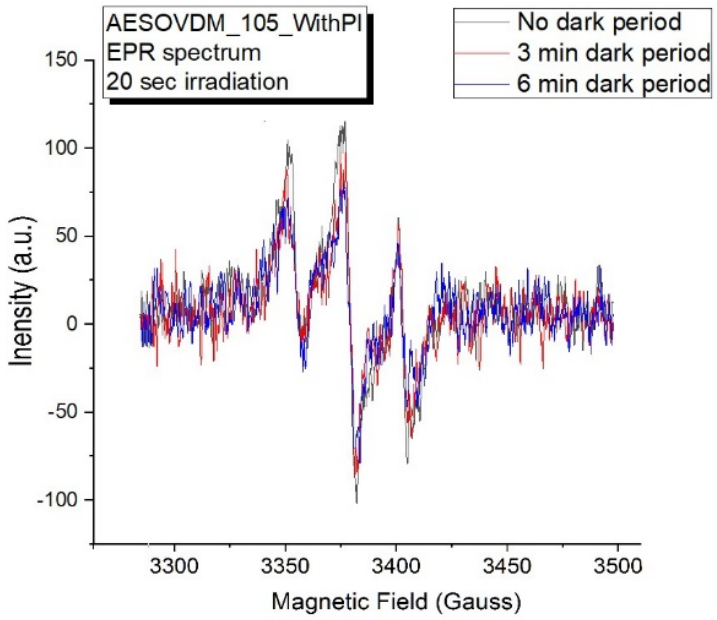

Figure 13. EPR results for cured AESO:VDM (1:0.5) samples containing a photoinitiator (PI) during UV irradiation and dark periods. Adapted from [9].

3. Correlation between Polymer Structure and Biosensor Performance

Among the various types of biosensors: electrochemical (amperometric, potentiometric, conductometric), optical, piezoelectric, thermal (calorimetric), and mechanical-amperometric biosensors are of greatest practical interest for bionanotechnology applications. They are employed for the detection of phenolic derivatives in aqueous environments for environmental monitoring.

In the case of an amperometric biosensor, where the electrochemical signal depends on the electroactive product of an enzymatic reaction, a supporting polymer matrix in the form of a film (Figure 14a) offers significant advantages over an incorporating polymer matrix (Figure 14b). A supporting film ensures a high local concentration of the enzyme at the working electrode surface, creating a high concentration of the electroactive reaction product near the electrode and thereby enhancing biosensor sensitivity. In contrast, with an incorporating matrix, the enzyme is dispersed throughout its volume, and a substantial portion of enzyme molecules is located at a considerable distance from the electrode surface. Consequently, a large fraction of the reaction product does not contribute to the electrochemical signal because it diffuses into the bulk solution. Thus, this method of enzyme immobilization is characterized by significantly lower sensitivity compared to the supporting matrix approach employed in this work.

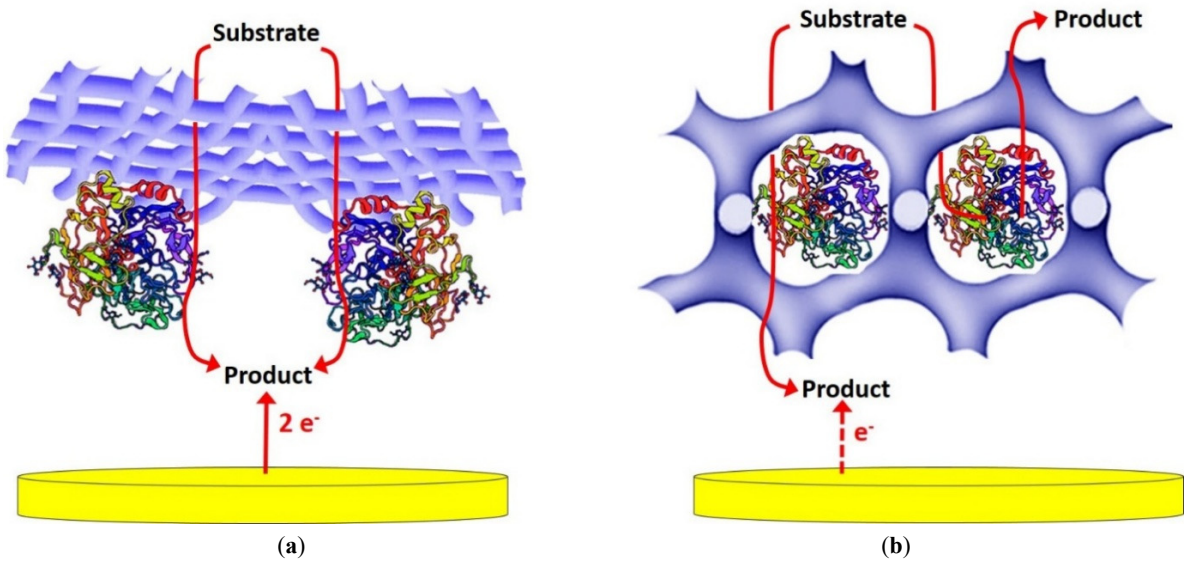

Figure 14. Schematic representation of enzyme immobilization on the electrode surface: (**a**) by fixation of the enzyme using a supporting polymer matrix (film), and (**b**) by incorporation of the enzyme within a polymer matrix.

The results of the comparative analysis of the structural characteristics (local free volume—LFV) of the studied polymers, along with the analytical performance of the constructed amperometric biosensors, are summarized in Table 8. The characterized samples were divided into two categories: samples with different morphologies and samples with the same morphology, as determined by PAS based on the temperature dependence of LFV for polymers and the LFV values at room temperature. Representative curves for the polymers are shown in Figure 15.

Analysis of Table 8 reveals a correlation in the "supporting polymer matrix—biosensor performance" system for samples with different morphologies. Specifically, an increase in local free volume (LFV) correlates with enhanced biosensor sensitivity. Since this correlation is observed across different types of polymers, both ureasil-based and photocross-linked, it may reflect a fundamental phenomenon. This suggests the presence of a topological mechanism—where the network structure or polymer topology contributes to effective enzyme immobilization in the biorecognition layer of an amperometric biosensor, with polymer network properties and topology playing a key role.

Table 8. Comparison of structural characteristics (local free volume, V_h) of the studied polymers, and analytical parameters (I_{max}—maximum current at substrate saturation, K_M^{app}—apparent Michaelis-Menten constant, sensitivity, linearity) of the constructed amperometric biosensors for the analysis of various analytes (ABTS and catechol).

Polymer	V_h (nm³)	I_{max} (μA)	K_M^{app} (mM)	Sensitivity ($A \cdot M^{-1} \cdot m^{-2}$)	Linearity, up to (mM)
Samples with different morphologies—ABTS					
Ureasil-1 [13]	0.112	4.45 ± 0.1	0.51 ± 0.02	1080	0.10
Ureasil-2 [13]	0.092	1.85 ± 0.1	0.38 ± 0.02	552	0.18
Ureasil-3 [13]	0.089	n/a	n/a	n/a	n/a
K0-fresh [5]	0.109	7.62 ± 1.7	0.64 ± 0.17	794	0.15
K0-aged [5]	0.121	10.96 ± 3.4	0.35 ± 0.14	1762	0.15
K4-fresh [5]	0.100	43.77 ± 2.7	0.045 ± 0.005	39817	0.04
K4-aged [5]	0.134	86.8 ± 0.9	0.030 ± 0.008	60413	0.06
ELO/10RD [6]	0.142	4.9 ± 0.19	0.36 ± 0.03	1673	0.15
ELO/30RD [6]	0.110	1.25 ± 0.17	0.11 ± 0.04	1234	0.10
ELO/PI [7]	0.155	0.34 ± 0.05	0.54 ± 0.07	233	0.10
ELO/10RD1/PI [7]	0.158	1.72 ± 0.03	0.35 ± 0.06	562	0.10
AESO/VDM 1:0.5 [7]	0.169	6.33 ± 0.19	0.29 ± 0.02	2452	0.10
Samples with the same morphology—ABTS					
CFA, <1 m^2/g [14]	~0.113	8.5 ± 0.3	0.35 ± 0.03	2890	0.20
CFB, 1448 m^2/g [14]	~0.113	7.5 ± 0.2	0.20 ± 0.01	4096	0.10
Catechol					
CFA, <1 m^2/g [14]	~0.113	3.9 ± 0.02	0.49 ± 0.01	1000	0.19
CFB, 1448 m^2/g [14]	~0.113	3.9 ± 0.02	0.45 ± 0.01	1137	0.19

Table 8. *Cont.*

Polymer	V_h (nm³)	I_{max} (μA)	K_M^{app} (mM)	Sensitivity ($A \cdot M^{-1} \cdot m^{-2}$)	Linearity, up to (mM)
ABTS—AESO series					
AESO [15]	0.158	5.43 ± 0.25	0.120 ± 0.019	1517	0.09
AESO:VDA 1:0.25 [15]	0.158	3.57 ± 0.23	0.158 ± 0.022	902	0.13
AESO:VDM 1:0.25 [15]	0.159	8.28 ± 0.20	0.326 ± 0.043	1608	0.13
Catechol—K series					
K2 [16]	~0.132	1.21 ± 0.04	0.32 ± 0.01	379	0.18
K5 [16]	~0.132	1.69 ± 0.09	0.41 ± 0.01	1900	0.18
K6 [16]	~0.132	1.79 ± 0.09	0.16 ± 0.01	735	0.18

Note: V_h values are reported at room temperature. Ureasil polymers with different precursors are designated as Ureasil-1 (100 mol.% precursor 1: 0 mol.% precursor 2), Ureasil-2 (30.8 mol.% precursor 1: 69.2 mol.% precursor 2), and Ureasil-3 (0 mol.% precursor 1: 100 mol.% precursor 2). Ureasil polymers containing chalcogenide clusters are denoted as K0-fresh (ureasil—2 months after synthesis), K0-aged (ureasil—1 year after synthesis), K4-fresh (ureasil/As_2S_3—2 months after synthesis), K4-aged (ureasil/As_2S_3—1 year after synthesis), K2 (ureasil/As_2S_3, 0.1 g As_2S_3), K5 (ureasil/S, 0.066 g S), and K6 (ureasil/S, 0.198 g S). Photocross-linked polymers, labeled ELO/10RD and ELO/30RD, consisted of epoxidized linseed oil (ELO), bisphenol A diglycidyl ether (RD) as a reactive diluent, and a 50% mixture of triarylsulfonium hexafluorophosphate in propylene carbonate as the photoinitiator (PI), corresponding to the reaction of ELO with 10 mol.% or 30 mol.% RD and 3 mol.% PI. ELO/PI consisted of ELO and 3 mol.% PI, while ELO/10RD1/PI consisted of ELO, 10 mol.% trimethylolpropane triglycidyl ether (RD1), and 3 mol.% PI. AESO refers to acrylated epoxidized soybean oil; VDA—vanillin diacrylate; VDM—vanillin dimethacrylate. The specific surface area (m^2/g) of the carbon fibers (CFA and CFB) [14,17] was determined according to the BET equation [18]. ABTS refers to 2,2′-azinobis(3-ethylbenzothiazoline-6-sulfonic acid), diammonium salt.

Furthermore, photocross-linked polymers with the same morphology based on acrylated epoxidized soybean oil (AESO), vanillin diacrylate (VDA), and vanillin dimethacrylate (VDM) in a 1:0.25 molar ratio, as well as ureasil polymers containing chalcogenide clusters (As_2S_3 and S): K2 (ureasil-As_2S_3, 0.1 g As_2S_3), K5 (ureasil-S, 0.066 g S), K6 (ureasil-S, 0.198 g S) exhibit similar behavior. For ureasil samples containing sulfur, a positive effect of a certain sulfur concentration on biosensor sensitivity is confirmed [16].

For photocross-linked polymers of the same morphology but different chemical composition, the observed differences in sensor sensitivity may be associated with the difference in acid dissociation constant (pK_a) between AESO:VDM and AESO:VDA. This affects the polymer matrix charge and, consequently, the access of the charged substrate (ABTS) and its electroactive product ($ABTS^{+\bullet}$) to the electrode surface via electrostatic interactions (Figure 16). Thus, a chemical mechanism (dependent on the chemical nature of the polymers) also contributes to effective enzyme immobilization in the biorecognition layer of amperometric biosensors when using polymers with identical morphology.

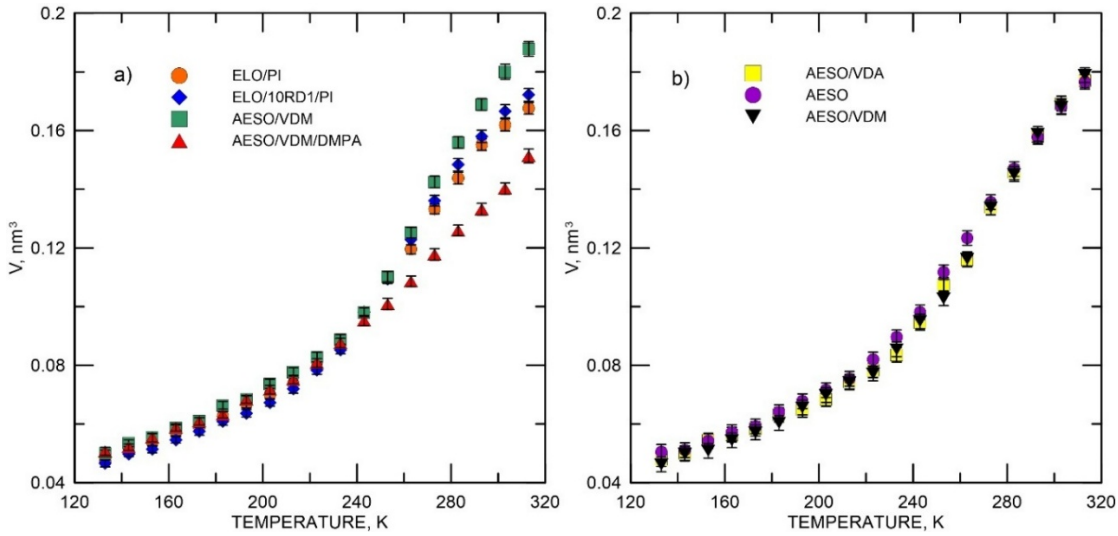

Figure 15. Local free volume (*o*-Ps lifetime) as a function of increasing temperature: (**a**) ELO/PI—circles, ELO/10RD1/PI—diamonds, AESO/VDM—squares, and AESO/VDM/DMPA—triangles (samples with different morphologies); (**b**) AESO—circles, AESO/VDA—squares, and AESO/VDM—triangles (samples with the same morphology). Adapted from [19].

It should be noted that the constructed amperometric biosensors based on the studied polymers, used as supporting enzyme matrices for environmental, biotechnological, and biomedical applications provide good agreement of biosensor measurements of phenolic derivatives with reference methods. In terms of key analytical characteristics, they are comparable to, and in most cases surpass, the performance of the closest known analogs worldwide.

The observed phenomena, explained within the established topological and chemical mechanisms of effective enzyme immobilization, depending on the morphology of the polymers, offer the possibility to tailor biosensor performance to specific practical applications. For instance, in samples with high analyte content (e.g., wastewater), a less sensitive biosensor is preferable to avoid multi-step dilution, which can compromise analytical accuracy. Conversely, for samples with low analyte concentrations (e.g., drinking water), the use of a highly sensitive biosensor with a wide linear range is critical.

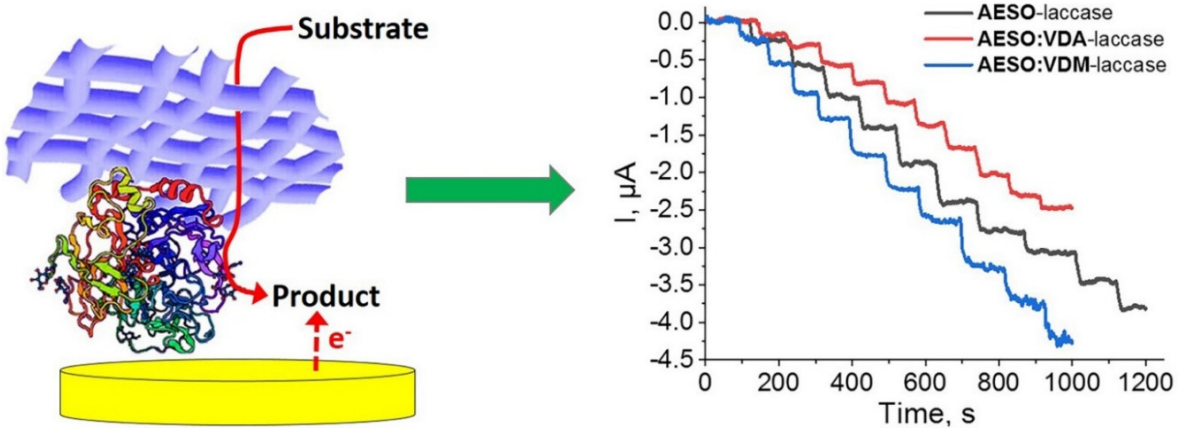

Figure 16. Schematic representation of the diffusion of the substrate and its electroactive product (for laccase: ABTS/$ABTS^{+\bullet}$) through the polymer voids when used as a supporting enzyme matrix. The supporting matrix maintains a high local enzyme concentration, resulting in high local production of the electroactive product of the enzymatic reaction near the electrode surface. Adapted from [15].

Design Principles for Polymer-Based Biosensors

Based on the relationships identified between polymer structure and biosensor performance, several general design principles can be formulated. Optimization of free volume is critical to balance enzyme accessibility with structural stability. Crosslinking density should be carefully controlled to regulate diffusion and mechanical integrity. Minimizing structural heterogeneity improves reproducibility, while polymer chemistry governs electrostatic interactions that influence substrate transport. Finally, surface-confined immobilization enhances sensitivity by maximizing the effective enzyme concentration at the electrode interface. Figure 17 shows a schematic representation of the design principles for polymer-based biosensors linking the polymer structure → free-volume generation → mass transport/analyte diffusion → biosensor signal generation.

These principles collectively provide a framework for the rational design of high-performance electrochemical biosensors.

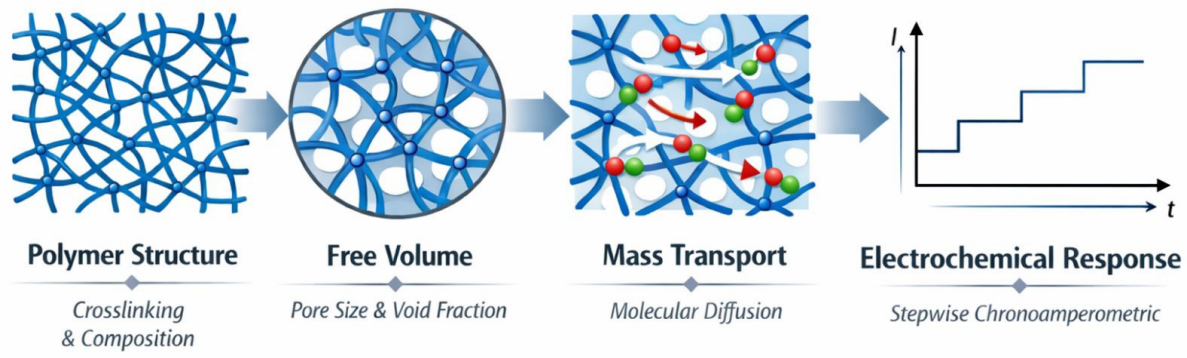

Figure 17. Schematic representation of the design principles for polymer-based biosensors linking the polymer structure → free-volume generation → mass transport/analyte diffusion → biosensor signal generation.

4. Conclusions

This review demonstrates that polymer microstructure and free volume are key determinants of electrochemical biosensor functionality. Positron annihilation spectroscopy provides a powerful tool for quantifying free-volume characteristics and linking them to material performance.

A fundamental correlation between free volume and biosensor sensitivity has been established, supported by both topological and chemical mechanisms of enzyme immobilization and mass transport. Control over polymer composition, crosslinking, and processing conditions enables precise tuning of these properties. In addition, photopolymerization and photodegradation processes significantly influence polymer microstructure and must be carefully controlled to achieve optimal performance.

Overall, the ability to engineer free volume in polymer matrices offers a universal strategy for improving biosensor sensitivity, selectivity, and operational stability. Future work should focus on extending these principles to a wider range of polymer systems and sensing applications.

Funding

This work was supported in part by the Ministry of Education and Science of Ukraine (projects Nos. 0125U002005 and 0125U002033) and National Research Foundation of Ukraine (project No. 2020.02/0100). T.K. also acknowledges the SAIA (Slovak Academic Information Agency) for a scholarship in the Institute of Physics of the Slovak Academy of Sciences in the framework of the National Scholarship Programme of the Slovak Republic. This work has also received funding through the MSCA4Ukraine project (grant No. 1128327), which is funded by the European Union.

Conflicts of Interest

The author declares no conflict of interest.

Use of AI and AI-Assisted Technologies

No AI tools were utilized for this paper.

References

1. Jean, Y.C. Positron annihilation spectroscopy for chemical analysis: A novel probe for microstructural analysis of polymers. *Microchem. J.* **1990**, *42*, 72–102. https://doi.org/10.1016/0026-265X(90)90027-3.
2. Kavetskyy, T.; Boev, V.; Ilcheva, V.; et al. Structural and free volume characterization of sol-gel organic-inorganic hybrids, obtained by co-condensation of two ureasilicate stoichiometric precursors. *J. Appl. Polym. Sci.* **2021**, *138*, e50615. https://doi.org/10.1002/app.50615.
3. Dahmouche, K.; Santilli, C.V.; Pulcinelli, S.H.; et al. Small-angle X-ray scattering study of sol-gel-derived siloxane-PEG and siloxane-PPG hybrid materials. *J. Phys. Chem. B* **1999**, *103*, 4937–4942. https://doi.org/10.1021/jp984605h.
4. Chen, H.M.; Jean, Y.C.; Lee, L.J.; et al. Positron annihilation study in inorganic-polymer nano-composites. *Phys. Stat. Sol. C* **2009**, *6*, 2397–2400. https://doi.org/10.1002/pssc.200982136.
5. Kavetskyy, T.S.; Smutok, O.; Gonchar, M.; et al. Ureasil-based polymer matrices as sensitive layers for the construction of amperometric biosensors. In *Advanced Nanotechnologies for Detection and Defence against CBRN Agents*; Petkov, P., Tsiulyanu, D., Popov, C., et al., Eds.; NATO Science for Peace and Security Series B: Physics and Biophysics; Springer: Dordrecht, The Netherlands, 2018; pp. 309–316. https://doi.org/10.1007/978-94-024-1298-7_30.
6. Kavetskyy, T.; Smutok, O.; Demkiv, O.; et al. Dependence of operational parameters of laccase-based biosensors on structure of photocross-linked polymers as holding matrixes. *Eur. Polym. J.* **2019**, *115*, 391–398. https://doi.org/10.1016/j.eurpolymj.2019.03.056.
7. Goździuk, M.; Kavetskyy, T.; Massana Roquero, D.; et al. UV-cured green polymers for biosensorics: Correlation of operational parameters of highly sensitive biosensors with nano-volumes and adsorption properties. *Materials* **2022**, *15*, 6607. https://doi.org/10.3390/ma15196607.
8. Královič, D.P.; Cifraničová, K.; Švajdlenková, H.; et al. Effect of aromatic rings in AESO-VDM biopolymers on the local free volume and diffusion properties of polymer matrix. *J. Polym. Environ.* **2024**, *32*, 2336–2349. https://doi.org/10.1007/s10924-023-03097-1.
9. Kavetskyy, T.; Zubrytska, O.; Stievenard, M.; et al. Complex network methods, PALS, ATR-FTIR and EPR study of photopolymerization. In *Nanotechnological Advances in Environmental, Cyber and CBRN Security*; Petkov, P., Achour, M.E., Popov, C., Eds.; NATO Science for Peace and Security Series B: Physics and Biophysics; Springer: Dordrecht, The Netherlands, 2025; pp. 265–284. https://doi.org/10.1007/978-94-024-2316-7_19.

10. Kavetskyy, T.S.; Zubrytska, O.V.; Matskiv, O.I.; et al. Photopolymerization and photodegradation of polymers after long-term UV light exposure. *Phys. Chem. Solid State* **2025**, *26*, 718–732. https://doi.org/10.15330/pcss.26.4.718-732.
11. Shim, H.-E.; Lee, B.-M.; Lim, D.-H.; et al. A comparative study of gamma-ray irradiation-induced oxidation: Polyethylene, poly (vinylidene fluoride), and polytetrafluoroethylene. *Polymers* **2022**, *14*, 4570. https://doi.org/10.3390/polym14214570.
12. Liu, S.; Li, Q.; Wang, J.; et al. Study on the post-irradiation oxidation of polyethylenes using EPR and FTIR technique. *Polym. Degrad. Stab.* **2022**, *196*, 109846. https://doi.org/10.1016/j.polymdegradstab.2022.109846.
13. Kavetskyy, T.; Kukhazh, Y.; Hoivanovych, N.; et al. On the correlation of network properties of polymer matrixes with parameters of electrochemical biosensors. *Acta Carpathica* **2024**, *1*, 105–116. https://doi.org/10.32782/2450-8640.2024.1.11.
14. Kavetskyy, T.; Smutok, O.; Demkiv, O.; et al. Microporous carbon fibers as electroconductive immobilization matrixes: Effect of their structure on operational parameters of laccase-based amperometric biosensor. *Mater. Sci. Eng. C* **2020**, *109*, 110570. https://doi.org/10.1016/j.msec.2019.110570.
15. Kavetskyy, T.; Smutok, O.; Goździuk-Gontarz, M.; et al. Impact of chemical composition of soybean oil and vanillin-based photocross-linked polymers on parameters of electrochemical biosensors. *Microchem. J.* **2024**, *201*, 110618. https://doi.org/10.1016/j.microc.2024.110618.
16. Kavetskyy, T.; Kukhazh, Y.; Demkiv, O.; et al. Organic-inorganic ureasil-based composites with sulfur for biosensors. In *Nanotechnological Advances in Environmental, Cyber and CBRN Security*; Petkov, P., Achour, M.E., Popov, C., Eds.; NATO Science for Peace and Security Series B: Physics and Biophysics; Springer: Dordrecht, The Netherlands, 2025; pp. 513–519. https://doi.org/10.1007/978-94-024-2316-7_39.
17. Smutok, O.; Kavetskyy, T.; Prokopiv, T.; et al. New micro/nanocomposite with peroxidase-like activity in construction of oxidases-based amperometric biosensors for ethanol and glucose analysis. *Anal. Chim. Acta* **2021**, *1143*, 201–209. https://doi.org/10.1016/j.aca.2020.11.052.
18. Brunauer, S.; Emmett, P.; Teller, E. Adsorption of gases in multimolecular layer. *J. Am. Chem. Soc.* **1938**, *60*, 309–319. https://pubs.acs.org/doi/10.1021/ja01269a023.
19. Kavetskyy, T.; Tuzhykov, A.; Fink, D.; et al. Positron annihilation and AI-technology for creation of novel biosensors. *J. Phys. Conf. Ser*. **2025**, *3149*, 012028. https://doi.org/10.1088/1742-6596/3149/1/012028.